DOI: 10.13009/EUCASS2019-83

Numerical simulation of ice accretion and consequent power loss estimation in wind turbine blades

Serkan Özgen, Ezgi Akyıldız**, Ayşe Meriç Berker*** and Ali Çakmak†*
**Professor*
Middle East Technical University, Dept. Aerospace Eng., 06800, Ankara, Turkey, serkan.ozgen@ae.metu.edu.tr
***Researcher, ***Senior Researcher*
BORUSAN-R&D, 34750, Ataşehir, Istanbul, Turkey, eakyildiz@borusan.com, aberker@borusan.com,
†Researcher
BORUSAN-ENBW, 34398, Sarıyer, Istanbul, Turkey, acakmak@borusanenbwenerji.com

Abstract

The aim of this study is to simulate atmospheric ice accretion on wind turbine blades and to estimate power losses. A computational tool is developed that comprises six modules, one for estimating the local flow velocity and the angle of attack using the Blade Element Momentum Method (BEM), one for solving the flow field employing the Panel Method, one for computing the droplet trajectories with the Lagrangian approach, a module for calculating the convective heat transfer coefficients using the Integral Boundary Layer equations, an ice accretion module utilizing Extended Messinger Model and a module calculating power production by using BEM.

1. Introduction

Ice accretion on wind turbine components, particularly the blades causes problems like vibration and severe reductions in power production. Therefore, it is important to simulate the location, distribution, shape and mass of ice forming on wind turbines in order to reduce the effects of icing.

Energy production companies, research institutes and universities have been addressing this problem with an increasing interest in the recent years. Numerical simulations have been attracting a large fraction of this interest. Although early simulations were done by using software developed for the aerospace industry, recent efforts are directed towards dedicated software for wind turbines.

This paper describes a dedicated, in-house computational tool to address ice accretion simulation on wind turbines and resulting losses. The computational tool has six modules; a module for estimating the local total flow velocity and the angle of attack using the Blade Element Momentum Method, a module for solving the flow field employing the Panel Method, a module for computing the droplet trajectories with the Lagrangian approach, a thermodynamical module for calculating the convective heat transfer coefficients using the Integral Boundary Layer equations, an ice accretion module utilizing Extended Messinger Model and a module calculating power production on blades by using the Blade Element Momentum Method.

Numerical simulations are performed for the AEOLOS 30 kW wind turbine geometry, the characteristics of which are given in Table 1. The flow and atmospheric conditions for the analyses are given in Table 2. The power production is calculated for the clean and ice contaminated blade sections by modifying the geometries by adding not only the ice thickness distribution but also the boundary-layer displacement thickness distribution to the geometry, so that the viscous flow effects are accounted for by using a weak-interaction approach.

DOI: 10.13009/EUCASS2019-83

Table 1: The characteristics of the AEOLOS 30 kW wind turbine

Property	**Value**
Airfoil	DU93-W-210
Rotational speed, Ω	120 rpm
Root chord, c_r	0.703 m
Tip chord, c_t	0.02 m
Rotor radius, r	6 m
Blade twist, θ	17.45°

Table 2: The flow and atmospheric conditions for the analyses

Property	**Value**
Wind speed, U	11 m/s
Liquid water content (LWC)	0.05 g/m^3
Droplet diameter (MVD)	27 microns
Ambient temperature, T_a	-10°C
Ambient pressure, p_a	95610 Pa
Exposure time, t_{exp}	60, 120, 180 min
Relative humidity (RH)	100 %

2. Methodology

In this section, the modules that comprise the computational tool and the methods used are briefly explained.

2.1 Blade Element Momentum Method

A number of blade sections (elements) are selected from the three dimensional blade geometry for the analysis, Figure 1. The Blade Element Momentum Method computes the local angle of attack (α) and relative wind speed (U_{rel}), i.e. resultant velocity due to rotation and wind [1]. These parameters are calculated using the wind speed (U), the axial and tangential induction factors (a and a'), the blade radius (r), the rotor rpm (Ω), rotor solidity (σ) and the blade twist (θ). The relative wind and the angle of attack at each blade element is calculated from [1]:

$$U_{rel} = \frac{U(1-a)}{\sin\varphi} \quad \textbf{(1)}$$

$$\alpha = \varphi - \theta_i \quad \textbf{(2)}$$

where φ is the angle of the relative wind:

$$\tan\varphi = \frac{U(1-a)}{\Omega r(1+a')} \quad \textbf{(3)}$$

and θ_i is the pitch angle of the i'th section.

DOI: 10.13009/EUCASS2019-83

The axial and tangential induction factors are given as follows:

$$a = \frac{1}{1+4\frac{sin^2\varphi}{\sigma c_l \cos\varphi}} \quad \textbf{(4)}$$

$$a' = \frac{a}{\lambda_r \tan\varphi} \quad \textbf{(5)}$$

with the local speed ratio λ_r defined as:

$$\lambda_r = \frac{\Omega r}{U} \quad \textbf{(6)}$$

The power produced by each blade element is calculated from:

$$dP = \Omega dQ \quad \textbf{(7)}$$

where the torque is given by:

$$dQ = \sigma\pi\rho\frac{U^2(1-a)^2}{sin^2\varphi}(c_l \sin\varphi - c_d \cos\varphi)r^2 dr \quad \textbf{(8)}$$

In equation (8), c_l and c_d are the lift and drag coefficients of the blade section calculated from panel method and boundary-layer solution. In order to calculate the power production of the turbine, equation (8) is integrated over the radius of the blade and then the integral is multiplied by the number of blades.

The local angle of attack and the relative wind speed are then provided to the Panel Method for the computation of the flow field. The developed computational tool is capable of analyzing blades with 20 individual sections. The current study is conducted using 10 sections, where each section is represented by 180 data points.

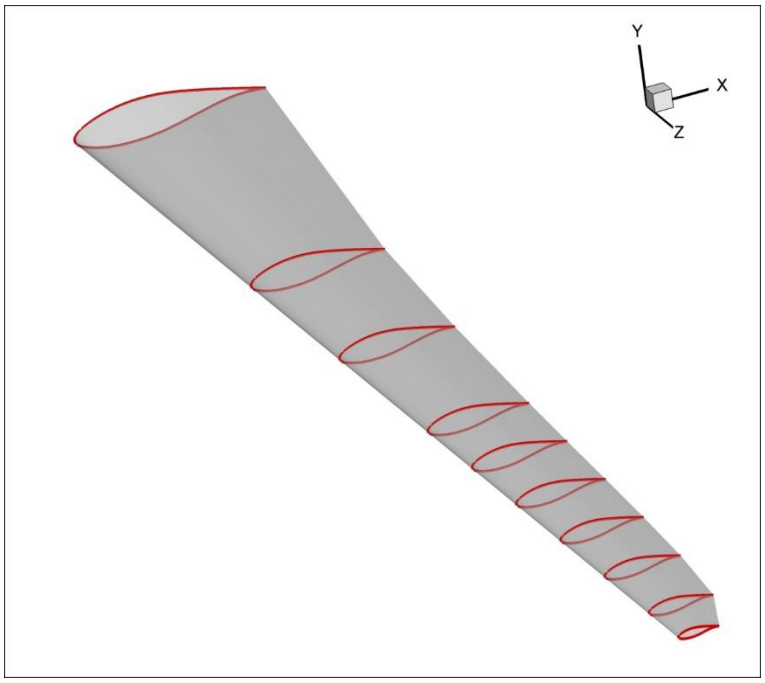

Figure 1: Blade elements selected for the analysis

2.2 Panel Method

Given the blade section geometry, velocity and angle of attack, the two-dimensional Panel Method solves the velocity distribution on the blade element and velocity components anywhere in the flow field. The velocity distribution on the blade element is fed as an input the boundary-layer calculations. Off-body velocity components are used to calculate the droplet trajectories.

DOI: 10.13009/EUCASS2019-83

2.3 Droplet Trajectories

Droplet trajectories are calculated using the Lagrangian approach integrating the two-dimensional equations of motion governing the motion of the droplets over time. This yields the droplet impingement zones and droplet collection efficiencies on the blade. For the details of these calculations, the reader is referred to Reference [2].

Geometry size and blade section leading edge radius have an important role on droplet trajectories and consequently on the impingement pattern. As the geometry and leading edge radius increases, the droplets tend to follow the streamlines, which result in fewer droplets impinging the surface over a narrow zone. Such an impingement pattern yields lower collection efficiency values. On the other hand, smaller geometries and sharp leading edge results in ballistic-like droplet trajectories resulting in higher number of droplets impinging over a wider zone. Such an impingement pattern yields higher collection efficiency values.

2.4 Boundary-layer calculations and convective heat transfer coefficients

The boundary-layer calculations are performed by solving the two-dimensional Integral Boundary Layer equation in order to obtain convective heat transfer coefficients over the blade section. In the laminar flow region, the method of Smith and Spaulding is used, while the formulation of Kays and Crawford is used in the turbulent region [2].

2.5 Ice Accretion Prediction; Extended Messinger Model

The ice shape prediction is based on the standard method of phase change or the Stefan problem. The phase change problem is governed by four equations: energy equations in the ice and water layers, mass conservation equation and a phase change condition at the ice/water interface [3]:

$$\frac{\partial T}{\partial t} = \frac{k_i}{\rho_i C_{pi}} \frac{\partial^2 T}{\partial y^2} \tag{9}$$

$$\frac{\partial \theta}{\partial t} = \frac{k_w}{\rho_w C_{pw}} \frac{\partial^2 \theta}{\partial y^2} \tag{10}$$

$$\rho_i \frac{\partial B}{\partial t} + \rho_w \frac{\partial h}{\partial t} = \rho_a \beta V_\infty + \dot{m}_{in} - \dot{m}_{e,s} \tag{11}$$

$$\rho_i L_f \frac{\partial B}{\partial t} = k_i \frac{\partial T}{\partial y} - k_w \frac{\partial \theta}{\partial y} \tag{12}$$

where θ and T are the temperatures, k_w and k_i are the thermal conductivities, C_{pw} and C_{pi} are the specific heats and h and B are the thicknesses of water and ice layers, respectively. In equation (11), $\rho_a \beta V_\infty$, $\dot{m}_{in}$ and $\dot{m}_{e,s}$ are impinging, runback and evaporating (or sublimating) water mass flow rates, respectively. Impinging mass is calculated as a product of liquid water content ρ_a, local collection efficiency β and total velocity V_∞. In equation (12), ρ_i and L_f denote the density of ice and the latent heat of solidification of water, respectively. The coordinate y is normal to the surface. In order to determine the ice and water thicknesses together with the temperature distribution at each layer, boundary and initial conditions must be specified. These are based on the following assumptions [3]:

i. Ice is in perfect contact with the airfoil surface, which is taken to be equal to the air temperature, T_a:

$$T(0,t) = T_s = T_a \tag{13}$$

ii. The temperature is continuous at the ice/water boundary and is equal to the freezing temperature:

$$T(B,t) = \theta(B,t) = T_f \tag{14}$$

iii. At the air/water (glaze ice) or air/ice (rime ice) interface, heat flux is determined by convection (Q_c), latent heat release (Q_l), cooling by incoming droplets (Q_d), heat brought in by runback water (Q_{in}), evaporation (Q_e), or sublimation (Q_s),, aerodynamic heating (Q_a), and kinetic energy of incoming droplets (Q_k):

$$\text{Glaze ice: } -k_w \frac{\partial \theta}{\partial y} = (Q_c + Q_e + Q_d) - (Q_a + Q_k + Q_{in}) \quad \text{at} \quad y = B + h, \tag{15}$$

$$\text{Rime ice: } -k_i \frac{\partial T}{\partial y} = (Q_c + Q_s + Q_d) - (Q_a + Q_k + Q_{in} + Q_l) \quad \text{at} \quad y = B \tag{16}$$

iv. Airfoil surface is initially clean:

$$B = h = 0, \; t = 0 \tag{17}$$

DOI: 10.13009/EUCASS2019-83

The system of equations given above yield an algebraic equation for rime ice, whereas an ordinary differential equations results for glaze ice:

$$\text{Rime ice: } B(t) = \frac{\rho_a \beta V_\infty + \dot{m}_{in} - \dot{m}_s}{\rho_r} t, \tag{18}$$

$$\text{Glaze ice: } \rho_g L_f \frac{\partial B}{\partial t} = k_i \frac{(T_f - T_s)}{B} + (Q_c + Q_e + Q_d) - (Q_a + Q_k + Q_{in}). \tag{19}$$

In order to calculate the glaze ice thickness as a function of time, equation (19) is integrated over time, using a Runge-Kutta-Fehlberg method. Transition from rime ice to glaze ice is smooth according to Extended Messinger Model formulation [3]. See [2] for further details.

3. Results and Discussion

The ice accretion problem on the AEOLOS 30 kW wind turbine is studied for an exposure of 180 minutes using a multi-step approach, where the geometry is modified with accreted ice every 60 minutes and the entire solution procedure repeated.

Figure 2 illustrates the ice formation on the AEOLOS 30 kW wind turbine blade after 180 minutes of exposure. As can be observed, the ice thickness and severity increases from blade root to blade tip, which is due to both increasing relative velocity thus increasing impingement rate and also reduction in size of the blade elements increasing the collection efficiency. It is known that the power production mostly occurs at outboard sections of a blade. This emphasizes the detrimental effect of ice formation on a blade.

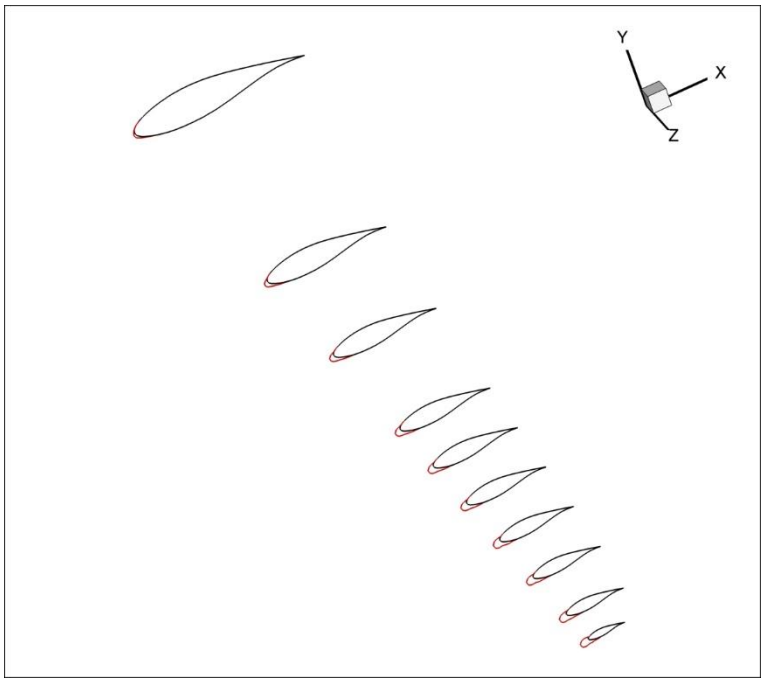

Figure 2: Ice formation on the blade elements of the AEOLOS 30 kW wind turbine

Figure 3 depicts the total ice mass accumulation on the blade as a function of exposure time. As can be seen, the ice mass is increasing almost in a linear trend with exposure time. Slight non-linearity is due to variation in the collection efficiencies due to ice formation.

Figure 4 shows the variation of turbine power production with exposure time. A rather interesting phenomenon is observed, which is the increase in power production in the first 60 minutes of exposure. This is the flap effect also mentioned by Han *et al* [4]. This can be explained as follows:

The rime ice formation typical of low air speeds and low LWC as in the current case are rather smooth in shape. This kind of ice formation resembles a leading edge flap deployed on an aircraft wing and conditions the airflow in a favourable manner. At earlier stages of exposure, ice is mostly rime on the blade sections, resulting in a slight increase in power production. As exposure increases however, the ice shape alters the blade profile shapes significantly and in

DOI: 10.13009/EUCASS2019-83

an unfavourable manner, possibly due to glaze ice formation that is known to degrade aerodynamic performance more severely than rime ice, resulting in steep reduction in power production as can be observed in Figure 4. Figure 5 shows an example to such rime ice formation, which is the ice geometry formed at $r = 4.5\ m$ (roughly 75% radial position) after 60 minutes exposure. The iced geometry is compared with a typical leading edge flap geometry, which reveals the resemblance of the ice geometry to that of a leading edge flap.

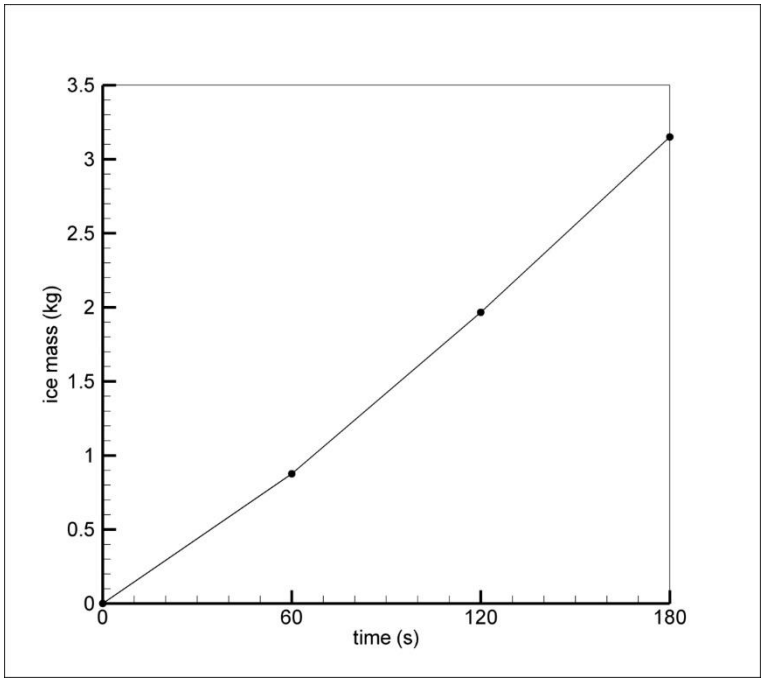

Figure 3: Variation of ice mass forming on the turbine blade as a function of exposure time.

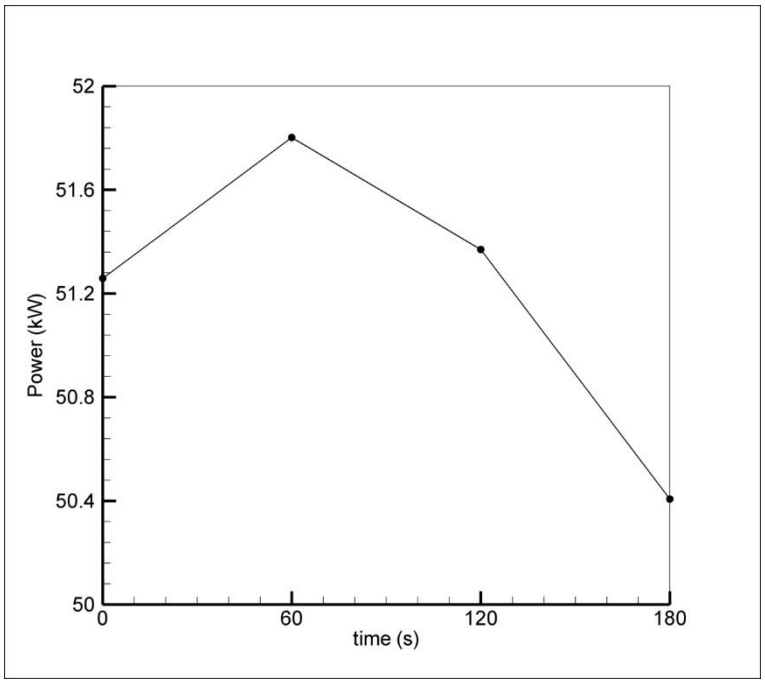

Figure 4: Variation of turbine power production as a function of exposure time.

DOI: 10.13009/EUCASS2019-83

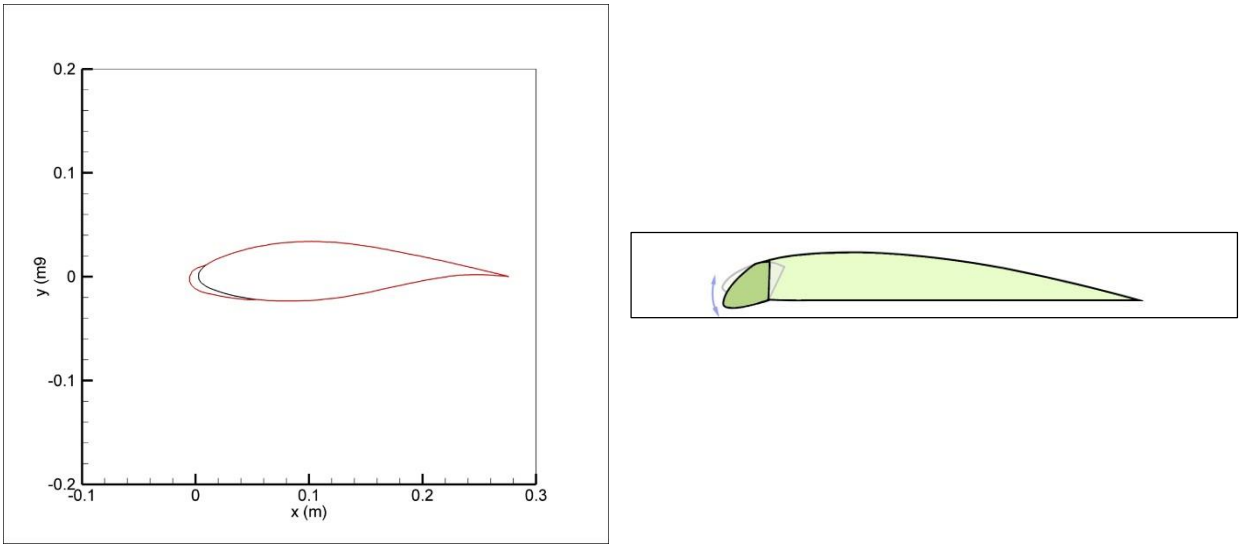

Figure 5: The ice formation (left) and a typical leading edge flap illustrating the “flap effect”

4. Conclusions

Atmospheric ice accretion on wind turbine blades and resulting power production losses are calculated using the developed in-house computational tool.

It is observed that ice thickness and its severity increases towards the blade tip. This is a point worth attention because the tip sections of a blade contribute more to power production than root sections. Therefore, power production is expected to be effected significantly due to ice formation. Any ice protection system that is envisaged therefore, should focus on blade tip sections in order to mitigate the effects of icing.

It is also shown that as exposure to icing conditions increases, the power production reduces steeply due to ice formation. At long exposure times, the ice thickness and shape significantly alters the blade shape, reducing the blade aerodynamic performance significantly. An exception to this, which is called the “flap effect” is also demonstrated, which is a phenomenon associated with rime ice at early stages of icing exposure.

As a result, the results can be regarded as encouraging, which is a motivation for further improvement. Potential areas of improvement may include a more accurate method for calculating aerodynamic performance, taking into account flow separation effects, in particular. It is a well-known fact that flow separation results in a sharp reduction in lift and an increase in drag, which may render more realistic power production loss estimations than what is presented in this study.

References

[1] Manwell, J.F., McGowan, J.G. and Rogers A.L. 2010. *Wing Energy Explained: Theory, Design and Application.* Wiley.
[2] Özgen, S. and Canıbek, M. 2009. Ice accretion simulation on multi-element airfoils using Extended Messinger Model. *Heat and Mass Transfer* 45(3):305-322.
[3] Myers, T.G. 2001. Extension to the Messinger Model for aircraft icing. *AIAA J* 39(2):211-218.
[4] Han, Y., Palacios, J. and Schmitz, S. 2012. Scaled ice accretion experiments on a rotating wind turbine blade. *J. Wind Eng. Ind. Aerodyn.* 109:55-67.